



A strategy for improving deactivation of catalytic combustion at low temperature via synergistic photocatalysis



Dong Jiang, Wenzhong Wang*, Ling Zhang, Ruihao Qiu, Songmei Sun, Yali Zheng

State Key Laboratory of High Performance Ceramics and Superfine Microstructure, Shanghai Institute of Ceramics, Chinese Academy of Sciences, PR China

ARTICLE INFO

Article history:

Received 5 September 2014

Received in revised form 11 October 2014

Accepted 14 October 2014

Available online 23 October 2014

Keywords:

Photocatalysis

Catalysis synergy

Remediation

Air purification

Surface hydroxyl

ABSTRACT

For practical catalytic combustion in heterogeneous catalysis, non-noble metal oxides with excellent low temperature activity as well as performance sustainability still remain challenging. Herein, semiconductor photocatalysis was introduced to address the problems. With greatly enhanced spectral response and low temperature reducibility, $\text{MnO}_x\text{-CeO}_2$ mixed oxide achieved convincing photo/thermo-catalysis synergy in formaldehyde abatement. This synergy is promising for utilizing infrared (IR) energy from sunlight and idle heat from daily illuminants. Moreover, the exhausted material after prolonged dark reaction presented inspiring self-remediation under in situ light irradiation. Catalytic cycles were thoroughly studied, unveiling the underlying mechanism based on photo-induced remediation. Roles of high valence metal ions, reaction intermediates and surface hydroxyls ($-\text{OH}$) have been in-depth and newly cognized. Given the day and night alternations in nature, our results may be instructive in designing reliable catalysts for efficient and sustainable catalytic combustion.

© 2014 Elsevier B.V. All rights reserved.

1. Introduction

Under consideration of both human health and environmental legislation, catalytic combustion of volatile organic compounds (VOCs) using transition metal oxides has been highly promising because of its technical and economic feasibility [1–5]. Recently, many efforts have been devoted to bringing down the starting temperature of various catalytic processes [6–8], as well as regenerating the exhausted catalyst after deactivation [9–12]. However, for the present the low temperature activity is still limited. Besides, additional post-treatments are generally required for material regeneration. For instance, O_2/Ar purging at 250°C and oxalic acid washing have been proposed to recover the used Co_3O_4 and three way catalysts (TWCs), respectively [10,13]. These requirements cannot be easily fulfilled and greatly hinder related civilian applications. A mild, convenient and in situ catalyst remediation for daily and practical VOCs abatement still remains a challenge.

During past decades, semiconductor photocatalysis has been widely attractive in environmental purification as well as artificial photosynthesis [14–18]. Superior to catalytic combustion which usually needs suitable conditions, it can operate at room temperature [19]. Moreover, compared with thermocatalysis,

photocatalysis is more effective for degradation of some recalcitrant organics, with few noxious intermediates but clean H_2O and CO_2 left behind [14]. In practice, the catalyst temperature is actually elevated as most light sources supply consecutive UV–vis–IR irradiation. Therefore, integrating mild thermocatalysis into photocatalysis should be promising for utilizing idle IR energy, which is helpless in driving most photocatalysis because of the energy limit. However, IR-induced solar heating is generally repulsive in photocatalysis, as it usually leads to severe lattice vibration, damaging the photon-to-electron conversion [20]. Recently, we proposed a feasible strategy to address above IR-related contradiction, by integrating solid state ionics into photocatalysis [21]. Within fluorite $\text{Ce}_{1-x}\text{Bi}_x\text{O}_{2-\delta}$ nanorods, the coupled electronic and ionic conduction help improve the negative temperature effect and integrate synergistic low temperature catalysis into solar energy utilization [21].

With photo/thermo-catalysis synergy, it has been proved that amazing enhancement can be achieved over CeO_2 -based catalysts in VOCs abatement, such as formaldehyde [21] and benzene [22]. However, for practical application the low temperature performance needs to be further improved. On the other hand, for practical catalytic combustion the material sustainability is another key point. There have been reports that Pt/TiO_2 shows better resistance to deactivation in photo/thermo-catalysis than in thermocatalysis alone [4,19]. However, the exact mechanism is still confusing and the cognition may be one-sided. It is worthwhile to explore the enhanced durability and in situ catalyst

* Corresponding author at: 1295 Dingxi Road, Shanghai 200050, PR China.

Tel.: +86 21 5241 5295; fax: +86 21 5241 3122.

E-mail address: wzwang@mail.sic.ac.cn (W. Wang).

regeneration in photo/thermo-catalysis synergy, for better understanding the underlying mechanism and designing desired catalysts.

Inspired by previous reports, introducing various heteroatoms into fluorite ceria can help promote the spectral response as well as the oxygen mobility [23–30]. The enhancements stem from intricate factors, including energy band modulation, abundant vacancies and a more open crystal structure. Herein, through an alkali-modified approach, $\text{Ce}_{1-x}\text{Mn}_x\text{O}_{2-\delta}$ solid solutions were prepared with moderate Mn contents ($x < 0.4$). Incorporation of Mn into CeO_2 helped improve the optical absorption and low temperature reducibility, simultaneously, inducing enhanced photo/thermo-catalysis synergy in the low temperature catalytic combustion of formaldehyde. Among the series of solid solutions, $\text{Ce}_{0.75}\text{Mn}_{0.25}\text{O}_{2-\delta}$ with the nominal 3:1 Ce/Mn atom ratio presented the most excellent performance and was selected as the representative for detailed discussion. During prolonged dark reaction, $\text{MnO}_x\text{-CeO}_2$ suffered gradual deactivation. However, the exhausted catalysts could be readily healed after in situ light irradiation, picking up more than 50% of the initialed activity. In-depth discussions unveiled the mystique in the photo-induced self-remediation. Reductions of high valence metal ions as well as accumulation of noxious reaction intermediates and inert surface hydroxyls led to the catalyst deactivation. Fortunately, the in situ light irradiation could help recover the reduced Mn^{3+} ions and free the blocked active sites, inducing inspiring self-remediation. More generally, given the day and night alternations in nature, our results are instructive in designing reliable catalysts for efficient and sustainable catalytic combustion, such as the round-the-clock air purification.

2. Experimental

2.1. Chemicals and characterization

All the reagents were of analytical purity and used as received from Sinopharm Reagent Co. Ltd. without further purification. The purity and crystallinity of as-prepared catalyst powders were characterized by powder X-ray diffraction (XRD) with a Rigaku D/MAX 2250V diffractometer using monochromatized Cu K α ($\lambda = 0.15418$ nm) radiation under 40 kV and 100 mA. The crystal size was estimated from the Scherrer equation, $D = (K\lambda)/(\text{FWHM} \cos \theta)$, where D is the crystal size, λ is the wavelength of the X-ray radiation and K usually is taken as 0.89, FWHM is the full width at half maximum in radian of the sample. The morphologies and microstructures characterizations were performed on the transmission electron microscopy (TEM, JEOL JEM-2100F, accelerating voltage 200 kV). Energy dispersive X-ray spectrum (EDX) was collected from an attached Oxford Link ISIS energy dispersive spectrometer. Diffuse reflectance spectra were obtained on a UV–vis spectrophotometer (Hitachi U-3010) using BaSO_4 as the reference. The N_2 -sorption measurements were performed at 77 K using a Micromeritics Tristar 3000 analyzer. Temperature programmed reduction (TPR) was performed (for each sample, 40 mg) on a ChemiSorb 2750 instrument equipped with a thermal conductivity detector, under a 10% H_2/Ar flow (30 mL min^{-1}) at a heating rate of $10^\circ\text{C min}^{-1}$. Raman spectra were recorded with a ThermoFisher spectrometer (DXR) with an excitation length of 532 nm. Fourier transform infrared (FTIR) spectra were recorded with a Nicolet iS10 FTIR spectrometer. X-Ray photoelectron spectroscopy (XPS) was employed to study the chemical states of the prepared samples. Spectra were performed on ESCALAB 250 (Thermo Scientific Ltd.) with a 320 mm diameter spot of monochromated aluminum K α X-rays at 1486.6 eV under ultrahigh vacuum conditions. The C 1s signal was used to correct the charge effects.

2.2. Preparation of catalysts

$\text{MnO}_x\text{-CeO}_2$ ($\text{Ce}_{0.75}\text{Mn}_{0.25}\text{O}_{2-\delta}$, denoted as CeMn-A) was synthesized by a facile Alkali-modified hydrothermal process. In a typical procedure, $\text{Ce}(\text{NO}_3)_3 \cdot 6\text{H}_2\text{O}$ (3 mmol) and KMnO_4 (1 mmol) were dissolved in deionized water (10 ml) and then mixed with a NaOH (6 M, 30 ml) solution. This mixture was kept stirring for 15 min with the formation of a milky suspension and then added into a 50 mL Teflon-lined autoclave with a stainless steel tank. The autoclave was finally subjected to the treatment at 110°C for 24 h. The precipitates obtained were rinsed with deionized water and anhydrous ethanol, and then freeze-dried and 60°C oven-dried in air successively. For comparison, pure CeO_2 (denoted as Ce-A) was prepared by the same process without KMnO_4 addition during the hydrothermal treatment.

2.3. Solar thermal measurement

100 mg powders of P25, CeO_2 and $\text{MnO}_x\text{-CeO}_2$ were dispersed in 6 ml anhydrous ethanol with the formation of suspension, respectively. Then, each suspension was dropwise and uniformly coated on a glass slide ($25 \text{ mm} \times 76 \text{ mm}$). A 275 W tungsten filament lamp was used to drying the slides. During the solar thermal measurement, a Xe lamp (500 mW cm^{-2}) was used as the light source, simulating the sunlight. A contact thermocouple was used to record the temperature variation. A white hard casing was covered outside the thermocouple to avoid the solar heating effect over the thermocouple itself.

2.4. Catalytic degradation test

The catalytic activities of the two samples (100 mg) were evaluated by the gas-phase degradation of formaldehyde (250 ppm), operated in a gas-closed vitreous reactor (capacity 650 mL) with a quartz window and a double-walled jacket with circulating water for temperature control. A 500 W Xe lamp (500 mW cm^{-2}) and different temperatures were used to simulate various catalytic conditions. The degradation process was monitored by the increment of CO_2 in the reactor by GC analysis (GC 7900, Techcomp) equipped with a TDX-01, 80–100 mesh packed column followed by a methane conversion furnace and a flame ionization detector (FID). It is worth noting that prior to any catalytic tests, the relevant condition must be maintained for several hours until the measured concentration of CO_2 remained unchanged to obtain equilibrium between adsorption and desorption, eliminating all adventitious interference factors.

2.5. Electrochemical analysis

The electrochemical measurements were performed on a CHI 660D electrochemical workstation (Shanghai Chenhua, China) using a standard three-electrode cell (quartz window, a working electrode, a platinum wire counter electrode, and a saturated calomel electrode (SCE) in saturated KCl as reference electrode). A Xe lamp (CHF-XM500) was used as light source equipped with various high-pass filters (400 nm, 450 nm and 510 nm) and positioned 6 cm away from the cell. To make a working electrode, as-obtained powders were deposited on a $15 \times 25 \text{ mm}$ fluorine-doped tin oxide (FTO) substrate by nafion coating. Briefly, 10 mg of catalyst was suspended in 400 μL of 1 wt% Nafion-ethanol solution and the mixtures were ultrasonically scattered for 15 min. Then, 150 μL of supernatant homogeneous solution was dropped on the FTO glass. After evaporation of the ethanol, the catalyst attached FTO glass was used as the working electrode. The cyclic voltammetry (CV) curves were recorded from +1.0 to -0.5 V vs. SCE, with a scanning rate of 50 mV s^{-1} . The current–time (i – t) curves were collected at

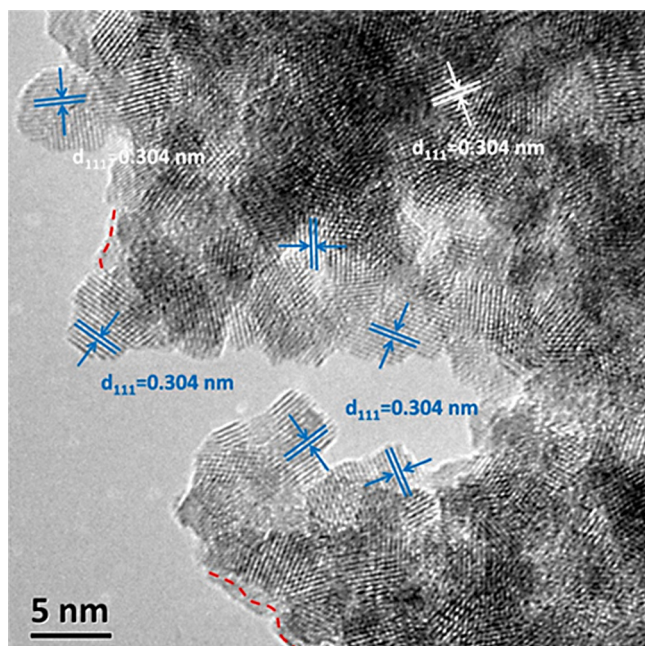


Fig. 1. High-resolution TEM image of $\text{MnO}_x\text{-CeO}_2$ ($\text{Ce}_{0.75}\text{Mn}_{0.25}\text{O}_{2-\delta}$, CeMn-A). Few amorphous regions are marked by red dotted lines. (For interpretation of the references to color in this figure legend, the reader is referred to the web version of this article.)

0.5 V vs. SCE under the irradiation of a Xe lamp equipped with a series of high-pass filters. During all of the measurements at room temperature, the electrolyte was 0.1 M Na_2SO_4 solution (pH 6.8).

3. Results and discussion

3.1. Characterization of catalyst

$\text{MnO}_x\text{-CeO}_2$ ($\text{Ce}_{0.75}\text{Mn}_{0.25}\text{O}_{2-\delta}$, CeMn-A) mixed oxide was prepared by an alkali-modified hydrothermal approach, with its X-ray diffraction (XRD) pattern readily indexed to a cubic fluorite structure (Fig. S1 in SI). Compared with the XRD pattern of CeO_2 (Ce-A), introduction of Mn ions induced evident shifts of diffraction peaks to higher angles. This variation is attributed to the partial substitution of Ce^{4+} (0.097 nm) by smaller Mn ions (0.067–0.053 nm), indicating the formation of $\text{MnO}_x\text{-CeO}_2$ solid solution. The broadening diffraction peaks of CeMn-A may suggest small size of nanostructures with low crystallinity and numerous defects. The average crystallite size of CeMn-A is calculated to be about 6.2 nm according to the Scherrer equation, using the strongest (1 1 1) diffraction peak at 28.5° 2θ . The BET surface area of CeMn-A is $241.5 \text{ m}^2 \text{ g}^{-1}$, three times larger than that of Ce-A ($81.2 \text{ m}^2 \text{ g}^{-1}$) (Fig. S2 in SI).

As indicated by TEM (Fig. S3 in SI), CeMn-A is a random packing of tiny particles, while Ce-A are gracile nanorods. The energy-dispersive X-ray (EDX) analysis gives the atom ratio of 3.16:1 for Ce/Mn, close to the nominal value 3:1. The high-resolution TEM (HRTEM) image (Fig. 1) further confirms the randomly stacked particles are separate in crystalline texture, with lattice fringes clearly identified. In the whole area, MnO_x of any crystal forms are not presented, and very few amorphous phases can be recognized. The fringes with lattice spacing of ca. 0.304 nm are assigned to the CeMn-A (1 1 1) planes, smaller than that of Ce-A (1 1 1) (0.311 nm). This further verifies the formation of solid solution. Besides, the particles are uniform in size, 4–6 nm (Fig. 1), which coincides well with the XRD results. These ultrafine particles will result in abundant defects on the catalyst surface such as dangling bonds and

vacancies, serving as active sites during various catalytic processes [25,31–33].

The chemical states of surface ions within the two materials were studied by X-ray photoelectron spectra (XPS) (Fig. 2). The surface Ce/Mn ratio from the XPS analysis is 2.98:1, close to the nominal value and EDX analysis. In Fig. 2a, six distinct characteristic peaks (u''' , u'' , u and v''' , v'' , v) are uniquely indexed to Ce^{4+} . Besides, the presence of Ce^{3+} ions (u' and v') can also be revealed in both samples [34]. Notably, there exist less Ce^{3+} ions on the surface of $\text{MnO}_x\text{-CeO}_2$ solid solution (5.34%) than pure CeO_2 (7.89%). Fig. 2b presents the Mn 2p XPS spectrum of $\text{MnO}_x\text{-CeO}_2$. Two main peaks located at 654.0 eV and 642.1 eV represent the two components Mn 2p_{1/2} and Mn 2p_{3/2}, respectively. Obviously, the broad Mn 2p peaks indicate the coexistence of Mn^{2+} (7.6%), Mn^{3+} (62.3%) and Mn^{4+} (30.1%) on the $\text{MnO}_x\text{-CeO}_2$ surface, though the binding energy of Mn 2p is reported to be unfixed due to the strong interaction between Mn and the CeO_2 matrix [23,35,36]. Given the charge conservation within the mixed oxide, it behoves the presence of low valence state Mn (Mn^{2+} and Mn^{3+}) to be balanced by decreasing Ce^{3+} , rationalizing the data from the Ce 3d XPS. Furthermore, as indicated by the Raman spectra (Fig. S4 in SI), introducing small Mn ions into ceria induced lattice contraction and abundant oxygen vacancies, though Ce^{3+} ions in $\text{MnO}_x\text{-CeO}_2$ decreased.

3.2. Evaluating the catalytic activity

As verified previously, ceria is capable of integrating synergistic catalytic combustion into photocatalysis [21,22]. However, pure ceria has limited photoresponse for solar energy utilization, and gets used to high temperature in thermocatalysis ($>100^\circ\text{C}$). Therefore, an all-round enhancement is required for the practical applications of catalytic combustion at mild conditions.

3.2.1. Extended and enhanced photoresponse

Insufficient light absorption in vis–NIR region hinders plenty of photocatalysts for further application, including ceria. As indicated in DRS (Fig. 3a), Ce-A hardly absorbs any vis–NIR light. After the introduction of Mn, CeMn-A presents a complete adsorption in the testing range, corresponding to its brownish color. However, enhanced vis–NIR absorption does not always induce photocatalysis, as light absorption is just an essential but not sufficient condition for the following catalytic processes. Catalyst excitation accompanying with energetic electrons and holes is required. Transient current–time (i – t) curves were recorded with various incident light (Fig. 3b). It is obvious $\text{MnO}_x\text{-CeO}_2$ electrode exhibits much enhanced transient current responses via on–off cycles of irradiation. The current response recedes with the increase of light wavelength. Notably, the CeMn-A electrode ($>510 \text{ nm}$) presents comparable current response to that of Ce-A under Xe lamp irradiation. The imperfect current switch during light on–off cycles in Fig. 3b may be attributed to the weak crystallinity of solid solution nanoparticles. In summary, CeMn-A presents greatly extended photoabsorption and enhanced photoresponse with charge carriers output. This should be promising for enhanced photocatalytic performance, though those electrons and holes may be not as active as expected.

3.2.2. Enhanced low temperature reducibility.

In view of utilization of either the IR energy from sunlight or the idle heat energy from daily illuminants, low temperature catalysis is required as both types of energy serve as mild heat sources [21]. The remarkable catalytic performance and oxygen storage capability (OSC) of CeO_2 originate from its repeatable $\text{Ce}^{4+}/\text{Ce}^{3+}$ cycles. However, the reduction of ceria is relatively sluggish, greatly hindering its low temperature application [25,37,38]. The reducibility of as-prepared CeO_2 and $\text{MnO}_x\text{-CeO}_2$ solid solution

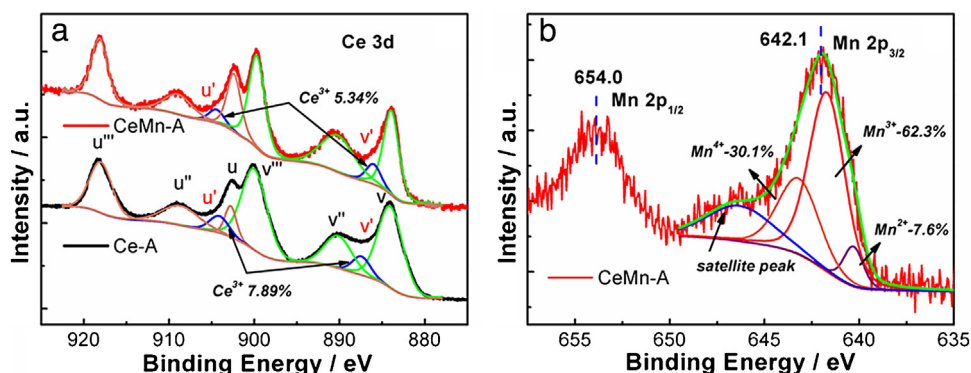


Fig. 2. (a) Ce 3d XPS spectra of CeO_2 (Ce-A) and $\text{MnO}_x\text{-CeO}_2$ (CeMn-A) samples. (b) Mn 2p XPS spectrum of $\text{MnO}_x\text{-CeO}_2$ (CeMn-A) sample.

was characterized by temperature programmed reduction in hydrogen (H_2 -TPR). As shown in Fig. 3c, the TPR trace of Ce-A displays a faint reduction peak at 268°C , ascribed to the removal of surface oxygen. Notably, with the same dosage (40 mg), CeMn-A gives a broad peak during $200\text{--}400^\circ\text{C}$. The TCD signal increase (>two orders of magnitude) of CeMn-A is much more than the BET surface area increase, three times. The giant enhancement of low temperature reducibility should be attributed to the more open lattice and abundant vacancies after introducing MnO_x . Besides, the intrinsic mutability of Mn ions is probably another important factor. The broad peak of CeMn-A comes from the close superposition of several reduction processes [35,39–41]. At least three subpeaks located at 218°C , 254°C and 332°C can be identified, corresponding to the reduction of high valence metal ions (Mn^{4+} , Mn^{3+} and Ce^{4+}). Moreover, CeMn-A presents a mysterious peak located around 482°C , which has never been clearly reported. Given the strong interaction between MnO_x and the CeO_2 matrix, we ascribe

this peak to the synergy between Mn and Ce ions within the solid solution.

We further tested the redox ability of above two samples under electrochemical conditions. After the introduction of MnO_x , the cyclic voltammograms of CeMn-A electrode present soaring redox peaks during the cyclic scanning, more than two orders of magnitude larger in current than that of Ce-A (Fig. 3d). Moreover, the cathodic peaks of CeMn-A corresponding to the electrode reduction are located at lower voltages (0.02 V, 0.39 V) than that of Ce-A (0.58 V), indicating that the reduction of Mn and Ce species within CeMn-A require much less energy [42]. That is, introduction of MnO_x greatly boosts the reducibility of resulted solid solution at mild conditions.

3.2.3. Low temperature photo/thermocatalysis synergy

Formaldehyde is one of the most common indoor air pollutants. Its continuous and recalcitrant emission from construction

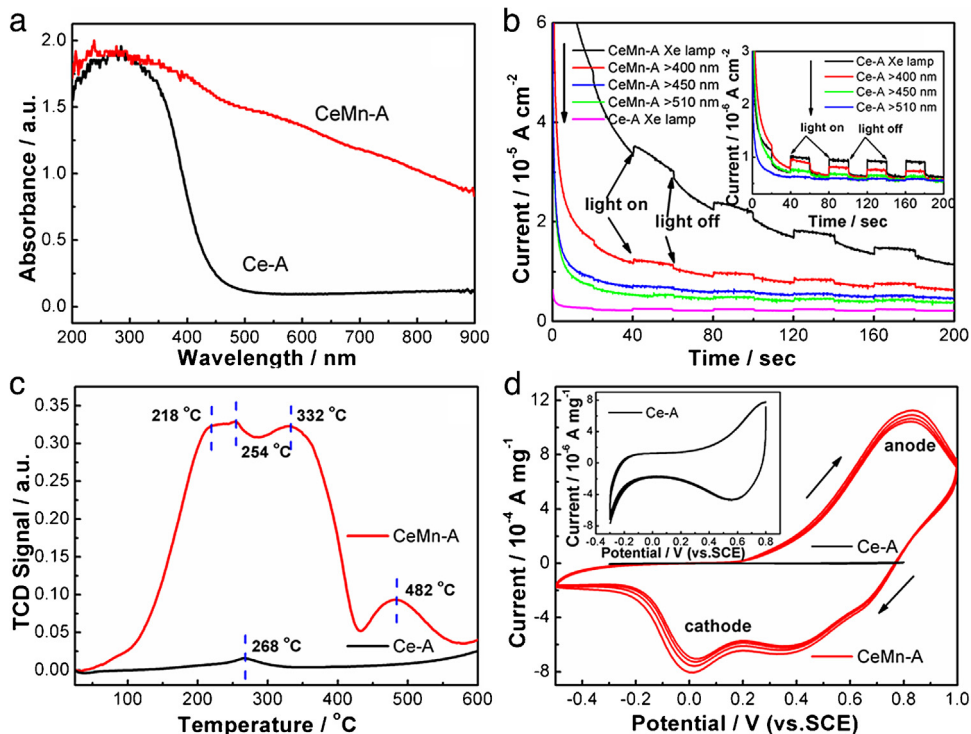


Fig. 3. (a) UV-vis diffuse reflectance spectra (DRS) of CeO_2 (Ce-A) and $\text{MnO}_x\text{-CeO}_2$ (CeMn-A) samples. (b) Current-time (i - t) curves of Ce-A (inset) and CeMn-A electrodes recorded at 0.5 V vs. SCE. The incident light of different wavelengths was obtained with a series of high-pass filters. (c) Temperature programmed reduction (H_2 -TPR) profiles of CeO_2 (Ce-A) and $\text{MnO}_x\text{-CeO}_2$ (CeMn-A) samples. (d) Cyclic voltammograms of Ce-A and CeMn-A electrodes in Na_2SO_4 electrolyte (0.1 M) with a scanning rate of 50 mV s^{-1} .

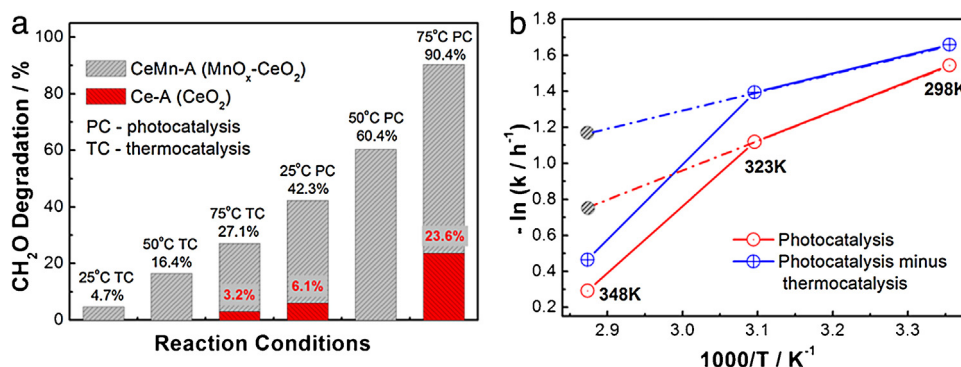


Fig. 4. (a) Statistics of formaldehyde degradation ratios after 3 h reaction over Ce-A and CeMn-A under different conditions. (b) The $-\ln k-T^{-1}$ Arrhenius plot showing the temperature dependence of reaction rate constant over CeMn-A. (For interpretation of the references to color in the text citation of this figure, the reader is referred to the web version of this article.)

and decorative materials has been extremely troublesome. Here, catalytic formaldehyde combustion is performed to evaluate the photo/thermo-catalysis synergy in MnO_x-CeO₂ solid solution. Before the experiment, the solar thermal effect was measured. For brownish MnO_x-CeO₂ with enhanced vis-IR absorption, promoted solar heating can be expected. The investigated objects were three glass slides coated with various catalyst powders (100 mg). After 5 min irradiation of Xe lamp (500 mW cm⁻²), the temperature of brownish MnO_x-CeO₂ rapidly increased from 25 °C to 75 °C, compared to 47 °C and 39 °C for CeO₂ and P25 (TiO₂) coated slides. With enhanced solar thermal collection, MnO_x-CeO₂ is promising for utilizing IR energy as a mild heat source in daily air purification.

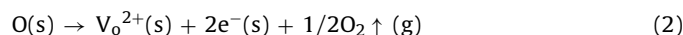
Catalytic formaldehyde (250 ppm) combustion was tested under different conditions to evaluate the photo/thermo-catalysis synergy (Fig. S5 in SI). In Fig. 4a, compared to pure CeO₂, MnO_x-CeO₂ presented much enhanced thermo- (8.5 times, 75 °C) and photo- (7 times, 25 °C) catalytic performance. Obviously, the enhancements are much more than the BET surface area increase. Moreover, the exposed {1 1 1} facets in CeMn-A have been widely suggested to be less reactive than {1 0 0} and {1 1 0}, which are predominantly exposed in Ce-A (Fig. S3 in SI) [24,25]. Therefore, the great enhancement over MnO_x-CeO₂ cannot be attributed to merely the BET and crystal facets related factors. Bearing above discussion in mind, it is reasonable to ascribe the promotion in CeMn-A to its enhanced light response and low temperature reducibility. Roughly, the photo/thermo-synergy was realized over CeMn-A, as the degradation ratio under the photo/thermo-condition exceeded the sum of that under thermo- and photo-conditions [19,22,43]. In Fig. 4a, 90.4% (75 °C PC) is much larger than 69.4%, the sum of 27.1% (75 °C TC) and 42.3% (25 °C PC). However, for a credible conclusion, the activity promotion from increased temperature must be removed according to the Arrhenius equation (Eq. (1)), where k and E_a represent the reaction rate constant and apparent activation energy, respectively [21].

$$k = A \exp\left(\frac{-E_a}{RT}\right) \quad \text{or} \quad \ln k = \ln A - \frac{E_a}{RT} \quad (1)$$

According to the Arrhenius equation, the reaction rate constant (k) will increase exponentially with temperature, because E_a can be treated as constant in a moderate temperature range. The reaction rate constants (k) were calculated (Fig. S5 in SI) and plotted appropriately to fit the equation (Fig. 4b). Notably, the $-\ln(k_{pc})-T^{-1}$ plot (red circles) presents a nonlinearity and an increasing slope (E_a) with the temperature. The increased E_a indicates that the greatly enhanced photocatalysis is not merely from the Arrhenius promotion. In that case, E_a will remain unchanged and the striated circle should have located along the dotted line (Fig. 4b), corresponding

to a smaller rate constant (k) [21]. Our conclusion seems to conflict with the general knowledge that, the lower the E_a the better the performance will be. However, this apparent discordance comes from an inaccurate derivation of the Arrhenius equation (Fig. S6 in SI). We went further to evaluate the photo/thermo-catalysis coupling, by deducting the thermo-contribution from the total synergy. In Fig. 4b, $-\ln(k_{pc} - k_{tc})$ is plotted vs. T^{-1} (blue circles), indicating similar nonlinearity and increasing E_a to that in red line. This result implies that, photocatalysis has been promoted by introducing thermocatalysis, confirming the mutual promotion between the two components in their low temperature synergy.

Different from the n -type TiO₂ based photocatalysis in which solar heating is usually repulsive, the negative temperature effect is improved within MnO_x-CeO₂ [4,21,22]. This difference can be explained by the coupled ionic and electronic conduction within MnO_x-CeO₂, inherited from fluorite ceria. Accompanying with the transport of lattice oxygen, the electronic conduction will be generated and coupled with the oxygen ion conduction (Eq. (2)). This kind of coupling will help improve the negative temperature effect, as elevated temperature does promote the ionic transport.



3.2.4. Reversible deactivation based on photo-remediation

For practical catalytic VOCs combustion, sustainable catalyst with convenient and in situ regeneration is urgently required. In our experiments, during prolonged dark reaction the MnO_x-CeO₂ catalyst suffered gradual deactivation. As shown in Fig. 5, after 30 successive dark cycles, the residuary activity over CeMn-A was less than 10% of the initial value. Nevertheless, the exhausted catalyst

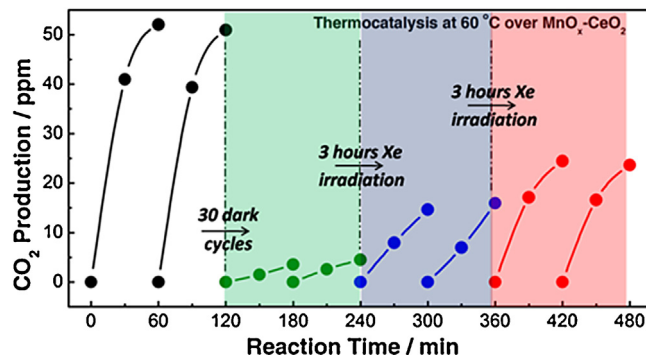


Fig. 5. Cycled formaldehyde degradation under thermocatalytic conditions (60 °C) over MnO_x-CeO₂ (CeMn-A). The first hour of each cycle was selected. To regenerate the exhausted catalyst, irradiation under a Xe lamp (500 mW cm⁻²) was performed.

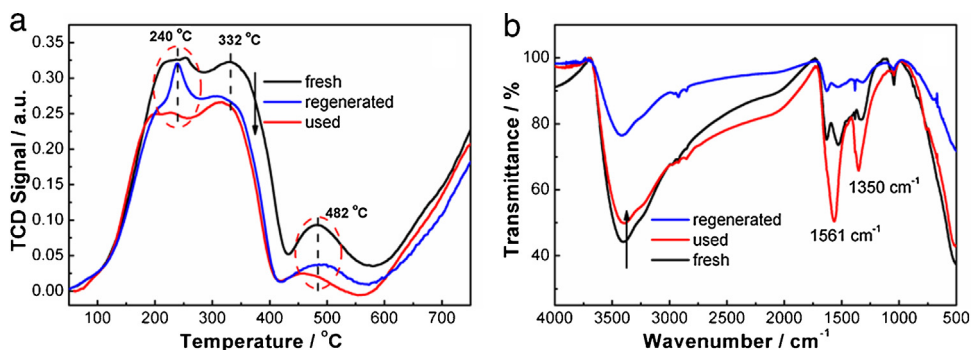


Fig. 6. Temperature programmed reduction (H_2 -TPR) profiles (a) and Fourier transform infrared (FTIR) spectra (b) of fresh, used and regenerated $\text{MnO}_x\text{-CeO}_2$ (CeMn-A) samples.

could be partly healed by light irradiation. After 3 h Xe lamp irradiation (500 mW cm^{-2} , 25°C), the used $\text{MnO}_x\text{-CeO}_2$ picked up about 30% activity compared to the beginning. The recovered activity further reached 50% after another 3 h irradiation (Fig. 5). However, the photo-induced remediation was limited and excess irradiation did not obviously bring about more improvements. We tested the dark deactivation and photo-remediation over the same sample for another two successive cycles. The in situ regeneration can be successfully achieved without recession (Fig. S7 in SI). In conclusion, the $\text{MnO}_x\text{-CeO}_2$ solid solution is in some sense a self-healing catalyst, which is based on the photoinduced performance recovering. Given the day–night alternations in nature, above catalyst should be promising for sustainable VOCs abatement.

3.3. Probing the origin of self-healing $\text{MnO}_x\text{-CeO}_2$

Catalytic VOCs combustion over metal oxides is widely accepted to follow the Mars–van Krevelen (MVK) cycle. Adsorbed object molecule is first oxidized by the lattice oxygen from the catalyst, and then gets reoxidized by gaseous O_2 in the environment [13,44]. So far, several mechanisms have been proposed to explain the deactivation of various metal oxide catalysts. One possibility is that deactivation is caused by the reductions of surface metal ions such as Mn^{4+} to Mn^{2+} and Cu^{2+} to Cu^+ , which cannot be readily recovered [9,45]. Another mechanism is the blocking of surface active sites by noxious reaction intermediates, such as carbonyl, carbonate, coke, etc. [4,19,43]. A third explanation is certain kind of surface poisoning from unavoidable water molecules [46–48]. In this

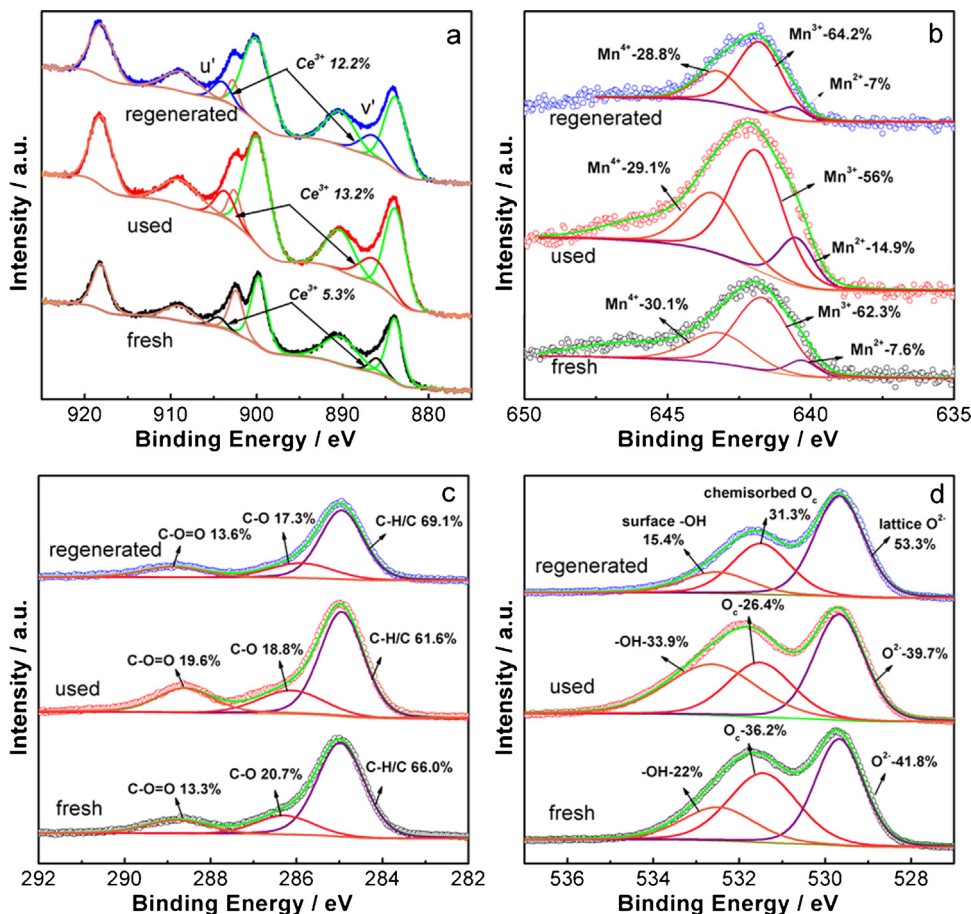
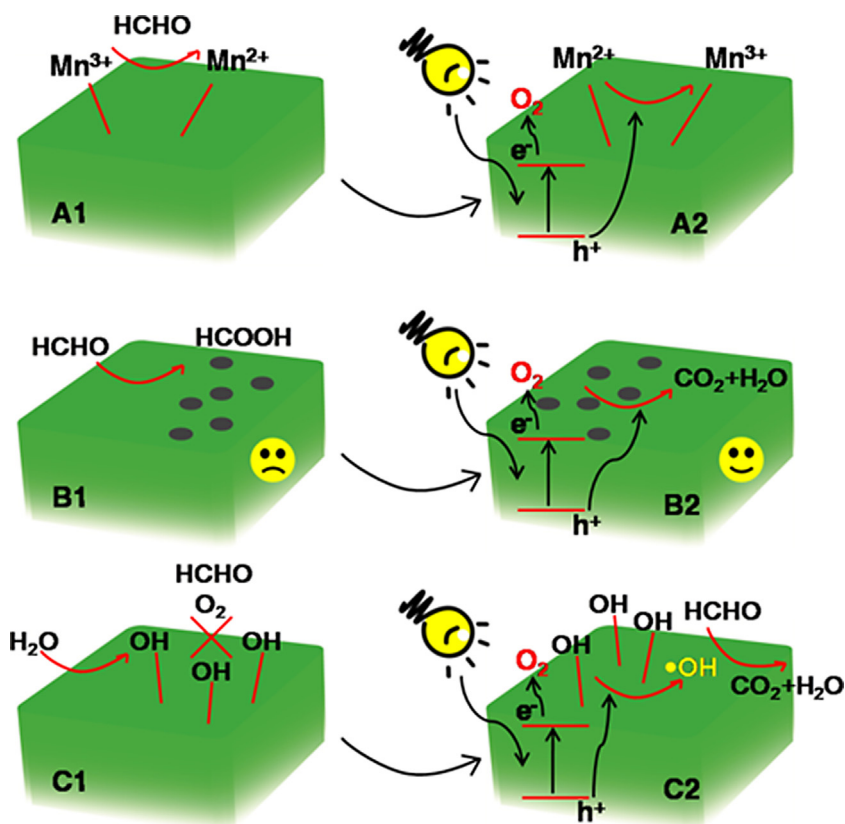


Fig. 7. XPS spectra of fresh, used and regenerated $\text{MnO}_x\text{-CeO}_2$ (CeMn-A) samples. (a) Ce 3d; (b) Mn 2p, the satellite peaks around 645–649 eV are not shown; (c) C 1s; (d) O 1s.



Scheme 1. Schematic diagram of dark deactivation and photocatalytic regeneration cycles within the $\text{MnO}_x\text{-CeO}_2$ system.

section, the origin of catalyst deactivation and regeneration are discussed in detail. To unveil relevant mechanism, the fresh, used (in dark reaction) and regenerated (after Xe lamp irradiation) samples were systematically studied.

3.3.1. Reversible valence of surface Mn ions

The XRD patterns of fresh, used and regenerated CeMn-A were studied (Fig. S8 in SI). All three samples presented almost overlapped fluorite peaks, indicating unchanged crystal structure. H_2 -TPR was used to provide a direct evidence of the low temperature reducibility. As shown in Fig. 6a, the used sample presented much depressed signal in the 200–600 °C range, compared to that of fresh CeMn-A . This difference indicates that, during the catalyst deactivation CeMn-A suffered a loss of various active sites for surface oxygen mobility. Given above discussion (Section 3.2.2), the depressed TPR came probably from the reductions of high valence metal ions (Mn^{4+} , Mn^{3+} and Ce^{4+}) and closely interacted Mn–Ce pairs. Interestingly, after 6 h of Xe lamp irradiation, the regenerated sample presented partial recovery in TPR signal. With the photo-remediation, the used sample mainly retook two TPR regions, as circled in Fig. 6a. The pinnacle around 240 °C indicates the Mn^{3+} specie was mostly recovered, which had suffered reduction during prolonged dark reaction. Another peak recovery is around 482 °C, indicating that the close Ce–Mn interaction was partly healed. Logically, the photo-induced remediation is ascribed to be photocatalytic. With appropriate optical excitation, strong oxidative species such as holes and hydroxyl radicals ($\cdot\text{OH}$) can be triggered to recover the reduced reaction sites.

The valence change is further verified by the XPS data. Fig. 7a shows the representative Ce 3d spectra of three CeMn-A samples. As indicated in Table S1 in SI, the molar ratio of trivalent cerium (Ce^{3+}) obviously increased from 5.3% to 13.2% during the deactivation. However, additional irradiation did not recover this

situation, indicating the irreversible reduction of Ce^{4+} . The Mn 2p spectra (Fig. 7b) present the valence variation of surface Mn ions during the thermocatalytic deactivation and photocatalytic regeneration. Notably (Table S1 in SI), the molar ratio of Mn^{4+} (30.1–29.1%) and Mn^{3+} (62.3–56%) decreased in the used sample, while the ratio of Mn^{2+} increased accordingly (7.6–14.9%). After irradiation, Mn^{3+} ions were mostly recovered back to 64.2%, accompanying with the decrease of Mn^{2+} (7%). In summary, the reductions of high valence ions (Ce^{4+} , Mn^{4+} , Mn^{3+}) contributed to the catalyst deactivation. The photocatalytic remediation partly recovered those ions (Mn^{3+}) and thus regenerated the exhausted catalyst.

3.3.2. Elimination of poisonous intermediates

It is widely accepted that recalcitrant reaction intermediates resulted from incomplete catalytic combustion can deactivate oxide catalysts [4,19,43]. Within our system, the role of reaction intermediates during the catalyst cycles was tracked by C 1s XPS analysis [49,50]. In Fig. 7c, three recognizable subpeaks located at 284.8, 286.2 and 288.8 eV are derived from C–H/C, C–O and O–C=O bonds, respectively. As summarized in Table S1 in SI, the O–C=O component on the surface of used example obviously increased (13.6–19.6%), probably indicating the partial oxidation of formaldehyde to formic acid, which is much less volatile. Surface coverage of these O–C=O intermediates blocked potential reaction sites and thus led to the deactivation. After the photocatalytic remediation, the surface O–C=O ratio decreased back to the initial level, 13.3%. Therefore, it is intelligible that elimination of noxious reaction intermediates also contributed to the catalyst regeneration. This intermediate-related viewpoint was further supported by the FTIR spectra. As shown in Fig. 6b, the used $\text{MnO}_x\text{-CeO}_2$ sharply displays two distinctive peaks, compared to that of the fresh and regenerated samples. The two intense absorptions located at 1350 cm^{-1} and 1561 cm^{-1} are diagnostically indexed to the symmetrical and

anti-symmetrical stretching vibration of carboxyl ($\text{O}=\text{C}=\text{O}$) groups [51,52]. This is consistent with the results from the C 1s XPS, featuring the role of reaction intermediates during the catalyst cycles.

3.3.3. Reversed role of surface bonded hydroxyl

Chemisorbed H_2O over the surface of transition metal oxides has been widely reported to be poisonous during various processes [47,48,53]. The dissociation of water (H_2O) molecule over the catalyst surface creates chemically bonded hydroxyl ($-\text{OH}$), blocking the adsorption of reactants and O_2 [8]. The competitive adsorption of H_2O inhibits the Mars–van Krevelen cycles. Furthermore, the reactivity of surface $-\text{OH}$ is proved to be much lower than that of lattice O, thus accelerating the catalyst deactivation [48]. The O 1s XPS was used to identify the coexistence of various O species [53–55]. As indicated in Fig. 7d, the ratio of surface $-\text{OH}$ greatly increased (22–33.9%) after the deactivation, while the ratio of chemisorbed O specie decreased (36.2–26.4%). Therefore, the surface poisoning from H_2O was also suggested to be important in the $\text{MnO}_x\text{--CeO}_2$ system. Notably on the surface of regenerated sample, there happened an intense reduction of $-\text{OH}$ groups (33.9–15.4%), as well as an obvious increase of lattice and chemisorbed O species.

In order to rationalize above surface changes, we propose to consider the reversed role of surface hydroxyls ($-\text{OH}$). On one hand, surface $-\text{OH}$ is negative in catalytic combustion for its site-blocking effect. On the other hand, it may be quite helpful in photocatalysis. Strong oxidative hydroxyl radicals ($\bullet\text{OH}$) evolved from uniting $-\text{OH}$ and photo-induced holes are indispensable in pollutants degradation. In our system, when the used sample was exposed to light irradiation, surface bonded hydroxyls ($-\text{OH}$) could be converted to abundant hydroxyl radicals ($\bullet\text{OH}$). When subjected to a new round of dark reaction, strong oxidative $\bullet\text{OH}$ on the surface would not only attack adsorbed organics, but free the blocked active sites for more reactive lattice and chemisorbed oxygen. That is, the photocatalytic remediation of used catalyst.

Through in-depth studies, the self-healing mechanism based on photocatalytic remediation can be well understood (Scheme 1). To summarize, during prolonged thermocatalysis, several key factors lead to the dark deactivation: (1) reduction of high valence metal ions (Mn^{4+} , Mn^{3+} , Ce^{4+}) on the surface greatly depress the catalyst reducibility (A1); (2) noxious reaction intermediates from incomplete organics decomposition block the reaction sites and poison the catalyst (B1); (3) unavoidable H_2O molecules produce inert surface bonded $-\text{OH}$ groups, further blocking the adsorption of reactants and O_2 , and accelerating the catalyst deactivation (C1). However, the exhausted catalyst can be partly healed by photocatalytic remediation: (1) photooxidation species mostly recover the reduced Mn^{3+} ions (A2); (2) noxious reaction intermediates are removed from the blocked active sites (B2); (3) photo-induced holes convert inert $-\text{OH}$ groups to strong oxidative $\bullet\text{OH}$, further contributing to the VOCs abatement and freeing the active sites (C3).

4. Conclusions

In summary, semiconductor photocatalysis was introduced into catalytic combustion over non-noble metal oxide catalyst. With much enhanced optical response and low temperature reducibility, $\text{MnO}_x\text{--CeO}_2$ mixed oxide achieved excellent catalysis synergy in formaldehyde abatement. Moreover, the exhausted material after prolonged dark reaction presented inspiring self-remediation with in situ light irradiation. In-depth studies unveil the mystique in the underlying synergy during the catalytic cycles, highlighting the photo-induced remediation. The unique roles of high valence metal ions, reaction intermediates as well as surface hydroxyls ($-\text{OH}$) have been illustrated in detail. More generally, given the

day and night alternations in nature, our results suggest appropriate photo/thermo-catalysis synergy may be instructive in designing reliable catalysts for efficient and sustainable catalytic combustion.

Acknowledgments

We acknowledge the financial support from the National Basic Research Program of China (2013CB933203) and the National Natural Science Foundation of China (51272269, 51272303, and 51102262).

Appendix A. Supplementary data

Supplementary data associated with this article can be found, in the online version, at <http://dx.doi.org/10.1016/j.apcatb.2014.10.040>.

References

- [1] A.K. Sinha, K. Suzuki, M. Takahara, H. Azuma, T. Nonaka, K. Fukumoto, *Angew. Chem. Int. Ed.* 119 (2007) 2949.
- [2] G.X. Chen, Y. Zhao, G. Fu, P.N. Duchesne, L. Gu, Y.P. Zheng, X.F. Weng, M.S. Chen, P. Zhang, C.W. Pao, J.F. Lee, N.F. Zheng, *Science* 344 (2014) 495.
- [3] S.J. Jiang, S.Q. Song, *Appl. Catal. B* 140 (2013) 1.
- [4] Y. Li, J. Huang, T. Peng, J. Xu, X. Zhao, *ChemCatChem* 2 (2010) 1082.
- [5] D. Li, Z. Chen, Y. Chen, W. Li, H. Huang, Y. He, X. Fu, *Environ. Sci. Technol.* 42 (2008) 2130.
- [6] N. Imanaka, T. Masui, H. Imadzu, K. Yasuda, *Chem. Commun.* 47 (2011) 11032.
- [7] S. Liang, F. Teng, G. Bulgan, R. Zong, Y. Zhu, *J. Phys. Chem. C* 112 (2008) 5307.
- [8] X. Xie, Y. Li, Z.Q. Liu, M. Haruta, W. Shen, *Nature* 458 (2009) 746.
- [9] P.G. Harrison, I.K. Ball, W. Azelee, W. Daniell, D. Goldfarb, *Chem. Mater.* 12 (2000) 3715.
- [10] W.G. Shim, S.C. Jung, S.G. Seo, S.C. Kim, *Catal. Today* 164 (2011) 500.
- [11] V.H. Vu, J. Belkouch, A. Ould-Driss, B. Taouk, *J. Hazard. Mater.* 169 (2009) 758.
- [12] X. Wu, H.R. Lee, S. Liu, D. Weng, *Ind. Eng. Chem. Res.* 52 (2012) 716.
- [13] J. Jansson, A.E. Palmqvist, E. Fridell, M. Skoglundh, L. Österlund, P. Thormählen, V. Langer, *J. Catal.* 211 (2002) 387.
- [14] M.R. Hoffmann, S.T. Martin, W. Choi, D.W. Bahnemann, *Chem. Rev.* 95 (1995) 69.
- [15] A. Fujishima, X. Zhang, D.A. Tryk, *Surf. Sci. Rep.* 63 (2008) 515.
- [16] A. Mills, R.H. Davies, D. Worsley, *Chem. Soc. Rev.* 22 (1993) 417.
- [17] X. Chen, S. Shen, L. Guo, S.S. Mao, *Chem. Rev.* 110 (2010) 6503.
- [18] D. Gust, T.A. Moore, A.L. Moore, *Acc. Chem. Res.* 42 (2009) 1890.
- [19] J.L. Falconer, K.A. Magrini-Bair, *J. Catal.* 179 (1998) 171.
- [20] S.H. Liu, E.J. Simburger, J. Matsumoto, A. Garcia, J. Ross, J. Nocero, *Prog. Photovolt.* 13 (2005) 149.
- [21] D. Jiang, W. Wang, E. Gao, L. Zhang, S. Sun, *J. Phys. Chem. C* 117 (2013) 24242.
- [22] Y. Li, Q. Sun, M. Kong, W. Shi, J. Huang, J. Tang, X. Zhao, *J. Phys. Chem. C* 115 (2011) 14050.
- [23] H. Chen, A. Sayari, A. Adnot, F. Larachi, *Appl. Catal. B* 32 (2001) 195.
- [24] C. Sun, H. Li, L. Chen, *Energy Environ. Sci.* 5 (2012) 8475.
- [25] X. Liu, K. Zhou, L. Wang, B. Wang, Y. Li, *J. Am. Chem. Soc.* 131 (2009) 3140.
- [26] C.J. Ren, L.N. Zhou, Y.W. Duan, Y.Q. Chen, *J. Rare Earths* 30 (2012) 1106.
- [27] A.D. Liyanage, S.D. Perera, K. Tan, Y. Chabal, K.J. Balkus, *ACS Catal.* 4 (2014) 577.
- [28] C.J. Mao, Y.X. Zhao, X.F. Qiu, J.J. Zhu, C. Burda, *Phys. Chem. Chem. Phys.* 10 (2008) 5633.
- [29] Z.L. Wang, G.R. Li, Y.N. Ou, Z.P. Feng, D.L. Qu, Y.X. Tong, *J. Phys. Chem. C* 115 (2011) 351.
- [30] Y.G. Wang, F. Wang, Y.T. Chen, D.F. Zhang, B. Li, S.F. Kang, X. Li, L.F. Cui, *Appl. Catal. B* 147 (2014) 602.
- [31] Y. Sun, Q. Liu, S. Gao, H. Cheng, F. Lei, Z. Sun, Y. Jiang, H. Su, S. Wei, Y. Xie, *Nat. Commun.* 4 (2013) 2899.
- [32] D. Jiang, W. Wang, E. Gao, S. Sun, L. Zhang, *Chem. Commun.* 50 (2014) 2005.
- [33] C.T. Campbell, C.H. Peden, *Science* 309 (2005) 713.
- [34] Q. Yuan, H.H. Duan, L.L. Li, Z.X. Li, W.T. Duan, L.S. Zhang, W.G. Song, C.H. Yan, *Adv. Mater.* 22 (2010) 1475.
- [35] Z. Wang, G.L. Shen, J.Q. Li, H.D. Liu, Q. Wang, Y.F. Chen, *Appl. Catal. B* 138 (2013) 253.
- [36] W.-J. Hong, S. Iwamoto, S. Hosokawa, K. Wada, H. Kanai, M. Inoue, *J. Catal.* 277 (2011) 208.
- [37] G. Dutta, U.V. Waghmare, T. Baidya, M. Hegde, K. Priolkar, P. Sarode, *Chem. Mater.* 18 (2006) 3249.
- [38] T. Yamamoto, A. Suzuki, Y. Nagai, T. Tanabe, F. Dong, Y. Inada, M. Nomura, M. Tada, Y. Iwasawa, *Angew. Chem. Int. Ed.* 46 (2007) 9253.
- [39] X. Wang, Q. Kang, D. Li, *Appl. Catal. B* 86 (2009) 166.
- [40] X. Tang, J. Chen, X. Huang, Y. Xu, W. Shen, *Appl. Catal. B* 81 (2008) 115.
- [41] D. Delimaris, T. Ioannides, *Appl. Catal. B* 84 (2008) 303.
- [42] X. Tang, B. Zhang, Y. Li, Y. Xu, Q. Xin, W. Shen, *Catal. Today* 93 (2004) 191.
- [43] J.C. Kennedy, A.K. Datye, *J. Catal.* 179 (1998) 375.

- [44] G. Bond, *Heterogeneous Catalysis: Principles and Applications*, 2nd ed., Clarendon Press, Oxford, 1987.
- [45] J. Jansson, *J. Catal.* 194 (2000) 55.
- [46] H. Zou, X. Dong, W. Lin, *Appl. Surf. Sci.* 253 (2006) 2893.
- [47] D. Gamarra, A. Martínez-Arias, *J. Catal.* 263 (2009) 189.
- [48] H.F. Wang, R. Kavanagh, Y.L. Guo, Y. Guo, G.Z. Lu, P. Hu, *Angew. Chem. Int. Ed.* 51 (2012) 6657.
- [49] E. Gao, W. Wang, M. Shang, J. Xu, *Phys. Chem. Chem. Phys.* 13 (2011) 2887.
- [50] D.R. Mullins, P.M. Albrecht, *J. Phys. Chem. C* 117 (2013) 14692.
- [51] J.P. Chen, L. Hong, S. Wu, L. Wang, *Langmuir* 18 (2002) 9413.
- [52] A.D. Weisz, A.E. Regazzoni, M.A. Blesa, *Solid State Ionics* 143 (2001) 125.
- [53] X. Du, X. Gao, Y. Fu, F. Gao, Z. Luo, K. Cen, *J. Colloid Interface Sci.* 368 (2012) 406.
- [54] J.-C. Dupin, D. Gonbeau, P. Vinatier, A. Levasseur, *Phys. Chem. Chem. Phys.* 2 (2000) 1319.
- [55] K.-i. Seo, P.C. McIntyre, H. Kim, K.C. Saraswat, *Appl. Phys. Lett.* 86 (2005) 082904.